Research Article Vol. 33, No. 18 / 8 Sep 2025 / Optics Express 38909
Optics EXPRESS

Time-of-flight signal processing for FTIR-based tactile sensors

JORGE GARCIA-PUEYO,[1,†,*] SERGIO CARTIEL,[1,†] EMMANUEL BACHER,[2] MARTIN LAURENZIS,[2] AND ADOLFO MUÑOZ[1]

[1] Universidad de Zaragoza, I3A, Zaragoza, Spain
[2] French-German Research Institute of Saint-Louis, 68301 Saint-Louis, France
[†] These authors contributed equally to this work.
[*] jorge.garciap@unizar.es

Abstract: Optical tactile sensors offer a promising avenue for advanced sensing and perception. We focus on frustrated total internal reflection (FTIR) tactile sensors that utilize time-of-flight (ToF) measurements. We analyze the complex behavior of ToF signals within optical waveguides in the time domain, where phenomena like internal reflections and scattering significantly influence light propagation, especially in the presence of touch. Leveraging this analysis, we develop a real-time processing algorithm that enhances FTIR tactile sensing capabilities, allowing for precise detection. We evaluate our algorithm on an OptoSkin sensor setup, demonstrating a significant improvement in multi-touch detection and contact shape reconstruction accuracy. This work represents a significant step towards high-resolution, low-cost optical tactile sensors, and advances the understanding of time-resolved light transport within waveguides and in scattering media.

1. Introduction

Tactile and pressure sensing are essential for interacting with the world and are present in most living beings. As such, this sensing modality has been developed artificially, for applications such as robotics, and there has been a proliferation of tactile sensors with different sensing principles and sizes.

The general adoption of tactile sensors is subject to challenges such as robustness, fabrication cost, deployment methodology and low-latency processing of the sensors. Large-area sensors are even more challenging due to the size of their coverage. Most of the large area tactile sensors are array-based, being composed of smaller sensor units (taxels) arranged in a surface, with cost proportional to surface area. In this regard, different technologies have been used, including piezo-resistive [1], capacitive [2], magnetic [3] or optical [4].

Among optical approaches for touch sensing, we can differentiate between those based on vision of surface deformation (TacTip [5], GelSight [6], Digit [7]) and those based on light transmission, which analyse the light changes due to contact but do not need the light detector to directly observe the contact point, lifting limitations on sensor design and setup. Light transmission sensors are based on diverse sensing principles like frustrated total internal reflection (FTIR) [8,9], liquid lenses [10] or optical fibers [11,12]. Recent works in tactile sensors based on light transmission have presented new approaches using optical time-of-flight (ToF) sensors together with optical waveguides for detecting touch [13,14]. In these setups, ToF sensors do not need to cover the whole surface area but only its perimeter, which, in practice, reduces fabrication time, cost and deployment time.

Of particular interest is the recent ToF FTIR-based tactile sensor, OptoSkin [14], that uses multiple ToF sensors on the perimeter of a planar optical waveguide. Light emitted by the ToF sensors propagates within the waveguide by total internal reflection (TIR). When an object makes contact with the waveguide, TIR is disrupted, causing light to scatter and escape. This

#570548 https://doi.org/10.1364/OE.570548
Journal © 2025 Received 11 Jun 2025; revised 23 Jul 2025; accepted 24 Jul 2025; published 4 Sep 2025

Optics EXPRESS

change in light behavior is captured by the detector element of the ToF sensor and enables the reconstruction of the touch position and pressure. Still, the original work where the OptoSkin sensor is presented overlooks most of the ToF signal structure within waveguides, and therefore demonstrates detection of just one or two simultaneous touches.

In this work, we devise a physically-based model to describe the structure of ToF signals inside waveguides, accounting for most optical phenomena, that becomes an analysis tool for ToF FTIR sensors. We then invert this model, and propose a real-time algorithm that processes the signal of ToF FTIR tactile sensors to greatly enhance contact and pressure detection. We evaluate its performance on a setup based on the recent OptoSkin sensor [14], demonstrating that our processing algorithm enhances the detection of simultaneous multiple contact points and improves reconstruction of contact area shapes.

2. Forward model: light propagation within optical waveguides

Large-area tactile sensors based on FTIR employ light emitters and detectors together with optical waveguides to direct light from one point to another by TIR. When something touches the waveguide, it produces FTIR and light is scattered. Light propagation within waveguides is subject to several optical phenomena that lead to signal degradation. This becomes particularly problematic for time-resolved signals, such as those obtained from ToF sensors. As a result, ToF FTIR sensors experience limitations when detecting touch and pressure with raw unprocessed signals, which we overcome in this paper by applying our algorithm to process them. In this section we give an overview of the optical phenomena of light propagation within waveguides, relating it to the LiDAR (Light Detection and Ranging) equation.

2.1. Time-of-flight sensors and the LiDAR equation

ToF sensors determine the distance between the sensor and an object by measuring the travel time of pulsed light. They are composed of a light emitter (e.g., a laser) and a detector (e.g., single-photon avalanche diodes, SPAD). The detector outputs histograms of photon counts over time (Fig. 1(a)). The histogram bin containing the highest peak of light is assumed to represent direct light reflecting from the object. The time value t_{peak} associated to such bin is used to compute the distance $d = t_{peak}\, c/2$ between the sensor and the object, being c [in m/s] the speed of light in air and the factor $1/2$ to account for light traveling forth and back.

Light measurements by ToF sensors can be described by the LiDAR equation [15], which quantifies the received photon counts (or light power) by the detector $Q(t)$ [in *Watts*] as

$$Q(t) = P_e(t) A \epsilon G(t) \beta(t) T(t), \tag{1}$$

where $P_e(t)$ [in *Watts*] is the emitted photons (or emitted power) by the laser, A [in m^2] is the aperture area of the detector, ϵ is the dimensionless system efficiency. The remaining terms describe the interaction of light with the medium: the geometric factor $G(t)$ [in m^{-2}] represents light divergence as it propagates, the transmittance term $T(t)$ [dimensionless] represents the attenuation of light due to absorption and scattering properties of the medium, and the backscattering coefficient $\beta(t)$ [dimensionless] quantifies the amount of light scattered back towards the detector from the medium at a specific range. For hard surfaces, $\beta(t)$ relates to the object's albedo at its distance and is zero beyond it.

2.2. Our forward model

When ToF sensors are coupled to waveguides, the temporal profile of light signals is different due to multiple light propagation effects (Fig. 1(b)-(e)). Therefore, detection of light peaks in such signals is suboptimal and prone to significant errors. To address this, we propose to define a forward model that describes the detected light signal from ToF sensors coupled to waveguides

Optics EXPRESS

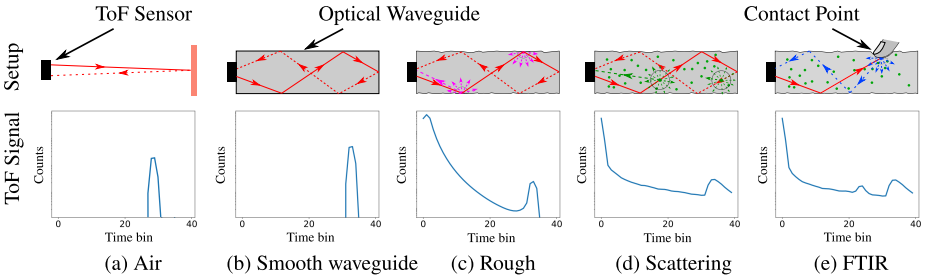

Fig. 1. Optical phenomena affecting light propagation in waveguides (up row) and the corresponding time-of-flight (ToF) signal (bottom row). (a) The ToF sensor emits a pulse of light that propagates through air, determining the object distance from the time-of-flight of the reflected light, which is easily distinguishable. (b) When coupled to a smooth dielectric waveguide, light travels efficiently through total internal reflection (TIR), allowing the ToF sensor to detect the waveguide's end accurately, which appears later due to the higher index of refraction of the waveguide. (c) If the waveguide's surface is rough, for instance due to fabrication imperfections, it produces some backscattering, increasing the signal at earlier times. (d) The presence of scattering particles (green dots) further disrupts light propagation, increasing backscattering and, thus, the signal complexity. (e) When there is a contact with the waveguide, it disrupts TIR, a phenomenon known as frustrated total internal reflection (FTIR), redirecting some light back to the sensor (blue path). Our forward model (Section 2) accounts for all these effects. We invert it (Section 3) to devise a signal processing algorithm that enables to identify the contact signal with respect to the rest of the optical phenomena signal.

and use it, in Section 3, to process the ToF signal for optimal detection of peaks of light associated to touch or pressure.

Unlike typical LiDAR applications that assume a single backscattering source (e.g., the atmosphere in the remote sensing field), our scenario involves multiple elements that can generate backscattering, like the waveguide's interface, waveguide's material and the object contacting the waveguide. Therefore, our proposed forward model extends the LiDAR equation [15] to include these multiple backscattering sources as

$$P_r(t) = Q_{int}(t) + Q_{vol}(t) + Q_{touch}(t) + N_{ms}(t) + N_a, \tag{2}$$

where $Q_{int}(t)$, $Q_{vol}(t)$ and $Q_{touch}(t)$ describe the power received due to backscattering interactions with the interface of the waveguide, the material composing the volume of the waveguide and the object touching the waveguide, respectively. Additionally, we include $N_{ms}(t)$ [in *Watts*] to account for received light due to multiple scattering and N_a[in *Watts*] for the ambient light (Section 2.6).

We decompose each component Q_i as

$$Q_i(t) = KG(t)\beta_i(t)T(t), \tag{3}$$

following the LiDAR equation (Eq. (1)), where K[in $Watts \cdot m^2$] summarizes the performance of the system depending on the emitted power $P_e(t)$, the area of the detector A and system efficiency ϵ, since they depend on the characteristics of the ToF sensor.

In the following sections, we describe in detail the geometry factor $G(t)$ (Section 2.4), the transmittance term $T(t)$ (Section 2.5) and the backscatter coefficients $\beta_i(t)$ for each backscattering source: interface of the waveguide $\beta_{int}(t)$ (Section 2.3), the volume of the waveguide $\beta_{vol}(t)$ (Section 2.5) or the object touching the waveguide $\beta_{touch}(t)$ (Section 2.7).

The term K is common to all the components $Q_i(t)$. Specifically, $Q_{touch}(t) = 0$ when there is not contact with the waveguide. While the contribution from $Q_{int}(t)$, $Q_{vol}(t)$ and $N_{ms}(t)$ depend

Optics EXPRESS

on the optical characteristics of the setup, which will remain stable, $Q_{touch}(t)$ reflects contact and pressure on the waveguide. Our goal is to detect variations of the time-of-flight measurements to obtain $\beta_{touch}(t)$, the touch backscattering, which we consider directly correlated with contact.

2.3. Dielectric waveguides

An optical waveguide consists on a dielectric slab, where the core region has a higher refractive index n_1 than both the medium above the core n_0 and the deposited substrate n_2 ($n_1 > n_2 \geq n_0$). If the medium above the core is air, $n_0 \approx 1$. These different refractive indices cause TIR, allowing light to propagate inside the waveguide due to light bouncing at both interfaces with an incident angle greater than the critical angle.

When the top and bottom boundaries of the waveguide are perfectly smooth and parallel, light travels by bouncing in a zig-zag pattern (Fig. 1(b)). Furthermore, the amount of backscattering produced by the interface would be negligible, $Q_{int}(t) \propto \beta_{int}(t) \approx 0$, except for the signal received due to the bounce in the end of the waveguide. However, fabrication processes might introduce micro-scale geometric irregularities in the interfaces, breaking the assumption of being smooth. Rough interfaces might introduce light leakage outside the waveguide and increase the amount of backscattering $\beta_{int}(t)>0$ so its effect, while probably still small, would not be negligible (Fig. 1(c)). Additionally, surface roughness also increases multiple scattering $N_{ms}(t)$.

2.4. Geometric factor

Due to light divergence as it propagates, there is a light intensity falloff that is proportional to the inverse squared distance. This phenomena is accounted for in the geometric factor

$$G(t) = \frac{1}{(c_1 t)^2}, \tag{4}$$

where $c_1 = c/n_1$ is the speed of light inside the dielectric waveguide and n_1 is the refractive index of the dielectric waveguide.

2.5. Scattering and extinction

Optical waveguides are composed of materials that may act as participating media, which differentiably interact with light, resulting in signal loss and aggravating the problem of non-straight light propagation (Fig. 1(d)).

We characterize optical waveguides by analyzing their optical parameters. Specifically, we use the absorption coefficient μ_a, which describes how much light is absorbed by the volume, and the scattering coefficient μ_s, which describes how much light interacts with the media, both in m^{-1}. We compute the extinction coefficient, $\mu_t = \mu_a + \mu_s$ [in m^{-1}] which describes the loss of intensity as light traverses a medium both from absorption and scattering. The extinction coefficient affects the power received by the detector through the transmittance term

$$T(t) = e^{-2\mu_t(c_1 t)}, \tag{5}$$

making the signal received by the detector lower, and where the factor 2 stands for the forth and back paths.

The scattering coefficient μ_s also affects the light propagation direction. This might produce backscattering, making light come back to the sensor and increasing the amount of light arriving to it at every timestep, $Q_{vol}(t) \propto \beta_{vol}(t) \propto \mu_s$, and slightly blurring the signal. Additionally, it will partially increase the overall multiple scattering $N_{ms}(t)$.

Optics EXPRESS

2.6. Ambient lighting

In addition, the detected signal will also include ambient light N_a, which comes from different sources such as sunlight and artificial lighting. Consequently, ambient light must be removed before evaluating the detected signal. In ToF sensors, the ambient signal at every timestep is estimated by collecting the light during the instant before the light pulse emission. Additionally, ToF sensors are usually equipped with optical filters that block light coming from wavelengths different from the wavelength of the emitter. In any case, ambient light is usually considered constant for a single histogram measurement, hence its independence from time in the forward model.

2.7. Frustrated total internal reflection

In optical waveguides, FTIR occurs when the outside medium (usually air) is replaced with another medium with a larger index of refraction. This medium interferes with TIR and causes light to exit the waveguide. When this new medium is highly scattering or even opaque, light scatters in all directions, reentering the waveguide and arriving to the detector (Fig. 1(e)). In FTIR-based sensors, this outside medium is a contact point, from which touch is detected. This effect is increased when the surface of the waveguide is deformable, so that pressure alters the surface orientation and hence the incoming light angle, which might be now below the critical angle. In our model, touch is represented by the backscatter coefficient $\beta_{touch}(t)>0$, which is in practice the value we want to obtain from the raw signal $P_r(t)$.

3. Inverse model: time-resolved signal correction

ToF sensors are able to detect objects in air because the associated light peak is easily distinguishable (Fig. 1(a)). However, as discussed in Section 2, the light signal structure changes drastically when ToF sensors are coupled to a waveguide. In this case, the detector of the ToF sensor collects light from multiple sources, making the default histogram-based distance estimation algorithms ineffective. In this section, we propose a signal correction algorithm to process the raw captured signal $P_r(t)$ (Fig. 2(b)) and isolate the signal coming from touch to estimate $\beta_{touch}(t)$ (Fig. 2(e)).

3.1. Baseline removal

ToF sensors cannot distinguish the source of the light they are detecting, so we have to isolate the signal received due to objects touching the waveguide. Initially, we perform a calibration step that consists on measuring the signal detected by the ToF sensor when no object touches the surface of the waveguide. We named this baseline signal $B(t)$ and it accounts for signal coming from ambient light N_a, from single backscattering after interacting with the interface of the waveguide $Q_{int}(t)$ (including the end of the waveguide that creates the final peak in Fig. 1(b)-(e)), from single backscattering after interacting with participating media of the volume of the waveguide $Q_{vol}(t)$ and from multiple scattering $N_{ms}(t)$ of multiple bounces light paths. The resulting signal after baseline removal $\hat{Q}_{touch}(t)$ (Fig. 2(c)), computed as

$$\begin{aligned}\hat{Q}_{touch}(t) &= P_r(t) - B(t) \\ &\approx P_r(t) - (Q_{int}(t) + Q_{vol}(t) + N_{ms}(t) + N_a),\end{aligned} \tag{6}$$

is an approximation of the signal received due to objects touching the waveguide. While each of the components (i.e. $Q_{int}(t)$, $Q_{vol}(t)$, $N_{ms}(t)$ and N_a) of the baseline signal $B(t)$ could be analytically modeled, these models would probably be too ideal compared to the realistic imperfections of non-uniform materials or fabrication irregularities. Therefore, a measured baseline is preferred. Note that a portion of ambient light N_a is already removed due to physical filtering previous to baseline subtraction.

Optics EXPRESS

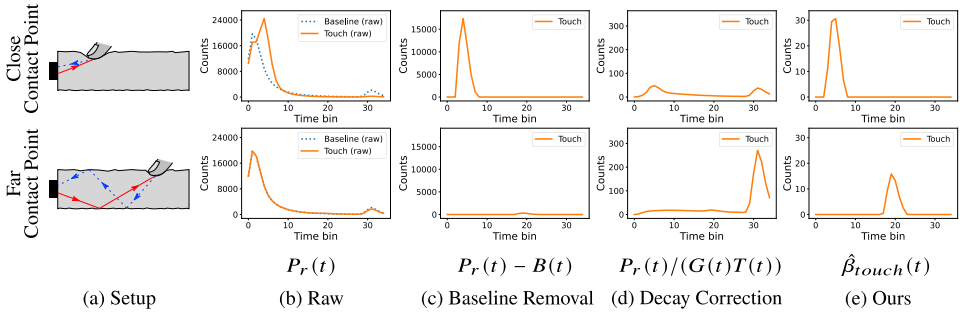

Fig. 2. ToF signals from a sensor coupled to a waveguide during two touch interactions. Each column corresponds to a different signal processing method, and each row shows a different contact location: close (top) and far (bottom) from the ToF sensor. (a) Diagram of the close and far contact points on the waveguide. (b) Raw: Unprocessed ToF measurements $P_r(t)$. The blue dotted lines show baseline signals (no touch), and the orange lines show signals during touch. For the close contact point, distinct peaks are observed corresponding to light entering the waveguide, contact interaction and waveguide end. For the far contact point, only the light entering the waveguide and the waveguide end peaks are visible. (c) Baseline removal: baseline signal $B(t)$ is subtracted from touch signal $P_r(t)$, revealing the peaks at contact locations. However, the intensity of the contact peaks vary significantly between the close one (clearly visible) and the far one (slightly visible). (d) Decay correction: the geometric factor $G(t)$ and extinction term $T(t)$ are compensated to normalize signal intensity over time. The close contact point becomes clearer but the far contact point remains suppressed. (e) Ours: combines baseline removal and decay correction, yielding consistent touch signal profiles $\hat{\beta}_{touch}(t)$ regardless of contact location.

3.2. Decay correction

We can assume that when $\hat{Q}_{touch}(t) \approx 0$, nothing is touching the waveguide, and when $\hat{Q}_{touch}(t)>0$, something is touching it. However, light presents an intensity decay dependent on the distance traveled by the light due to the geometry factor $G(t)$ and the transmittance term $T(t)$ (Sections 2.4 and 2.5). As a consequence, objects closer to the sensor will appear brighter than the ones further, as seen when applying only baseline removal in Fig. 2(c).

To ensure that touches at different distances produce signals of comparable magnitudes, it is necessary to account for the light decay, that depends on the distance traveled by light, as

$$\hat{\beta}_{touch}(t) = \frac{\hat{Q}_{touch}(t)}{G(t)T(t)} = \hat{Q}_{touch}(t)\frac{(c_1 t)^2}{e^{-2\mu_t(c_1 t)}}. \tag{7}$$

This approach compensates for the light intensity falloff observed in the raw signal $P_r(t)$ (Fig. 2(b)) and, when applied on the signal after baseline removal $\hat{Q}_{touch}(t)$, the processed signal $\hat{\beta}_{touch}(t)$ (Fig. 2(e)) is sufficiently consistent for automatic extraction of touch information. Note that just applying decay correction on the raw signal is not enough since the touch signal is still mixed with the baseline signal and far contact points are not clearly visible (Fig. 2(d), bottom row).

3.3. Implementation

We describe the implementation of our signal correction processing in Algorithm 1. The inputs are the raw captured signal $P_r(t)$, a previously acquired baseline signal $B(t)$ and known parameters of the optical setup (bin temporal resolution Δt of the ToF histogram, refractive index n_1, absorption coefficient μ_a and scattering soefficient μ_s of the waveguide's material). We first perform baseline removal (Section 3.1) to isolate the touch signal $\hat{Q}_{touch}(t)$, followed by decay

Optics EXPRESS

correction (Section 3.2) to normalize signal intensity across different distances. A more detailed analysis of the theoretical and experimental time complexity of our algorithm is provided in Supplement 1, Section 1.

Algorithm 1. Our time-resolved signal correction

Input: $P_r(t), B(t), \Delta t, n_1, \mu_s, \mu_a$
Output: $\hat{\beta}\_touch$

$c_1 \leftarrow c/n_1$ ▷ Speed of light inside the waveguide
$\mu_t \leftarrow \mu_s + \mu_a$ ▷ Extinction coefficient (Section 2.5)
$\hat{\beta}\_touch \leftarrow$ vector(size_of(P_r)) ▷ Create empty vector
for $i = 1$ to size_of(P_r) **do**
  $t \leftarrow i\,\Delta t$ ▷ Time t of bin i
  $G \leftarrow 1/(c_1 t)^2$ ▷ Geometric factor (Eq. 4)
  $T \leftarrow e^{-2\mu_t (c_1 t)}$ ▷ Transmittance term (Eq. 5)
  $\hat{q}_{touch} = P_r[i] - B[i]$ ▷ Baseline removal for bin i (Eq. 6)
  $\hat{\beta}\_touch[i] \leftarrow \hat{q}_{touch}/(GT)$ ▷ Decay correction for bin i (Eq. 7)
end for
return $\hat{\beta}\_touch$

4. OptoSkin and tactile maps

Our analysis and modeling of light propagation within waveguides (Section 2), along with the proposed signal correction algorithm (Section 3), are general and broadly applicable to any light sensor embedded in a volumetric medium. While this paper focuses on optical tactile sensors based on TIR or FTIR [4,8,9,13,16–19], the underlying approach can also be extended to other domains where light transport in scattering or refractive media plays a critical role, for instance underwater imaging [20–22] or detection through fog [23].

We choose to assess its performance (Section 5) on the ToF FTIR-based OptoSkin sensor [14]. In this section, we describe our experimental OptoSkin setup and the process to generate tactile maps to represent touch on the waveguide surface.

4.1. Experimental setup

We build our OptoSkin setup following the original work [14], strategically placing ToF sensors along the edges of the waveguide. As shown in Fig. 3, for the experiments, we placed six ToF sensors around a square waveguide with a size of $300mm \times 300mm$ and a thickness of $5mm$. The waveguide consists of a commercial two-component transparent soft silicone material (Troll Factory, Type 19, TFC4190-T19 [24]) with the following optical characteristics: refractive index of $n_1 = 1.4$, scattering coefficient of $\mu_s = 0.6cm^{-1}$, and absorption coefficient of $\mu_a = 0.14cm^{-1}$. See Supplement 1, Section 3 for more information on the waveguide's silicone material preparation and physical properties.

The positions of the sensors were chosen to ensure a comprehensive coverage of the tactile area by at least one sensor. We utilized the TMF8828 ToF sensor from AMS-OSRAM [25], which integrates a low-power pulsed VCSEL (vertical cavity surface-emitting laser diode) and SPAD technology within a single module. Additionally, it features an electronic control unit enabling the configuration of the sensing zones of the SPAD array (binning) and the processing and formatting of data (time-of-flight histograms) to be transmitted to an external device via an I2C bus. The binning on sensor level is used to reduce the overall data acquisition, processing and transmission time.

The key optical parameters of the TMF8828 ToF sensor are the bin temporal resolution, the field of illumination (FoI) and field of view (FoV). The bin temporal resolution is $\Delta t \approx 100ps$,

Optics EXPRESS

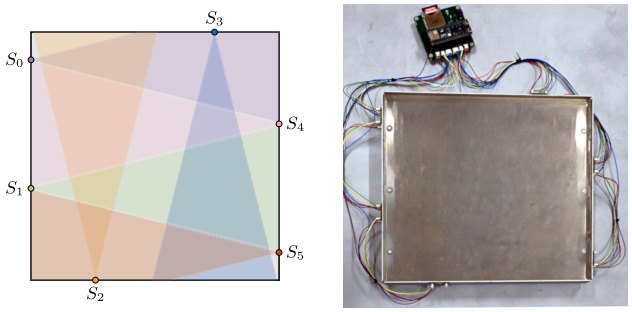

(a) (b)

Fig. 3. Sensor layout (a) and image (b) of our OptoSkin setup used in the performance experiments (Section 5). Six ToF sensors ($S_0, \ldots, S_5$) are strategically placed around a $300mm \times 300mm$ waveguide to ensure a comprehensive sensor coverage. The waveguide consists of a $5mm$ thick soft silicone rubber waveguide layer molded onto an aluminum substrate.

which is equivalent to a distance resolution (in air) of $\Delta d = \Delta t \frac{c}{2} = 1.5cm$. When coupled to a waveguide, the equivalent distance resolution has to take into account the refractive index as $\Delta d' = \Delta t \frac{c_1}{2} = \Delta t \frac{c}{2n_1} \approx 1.1cm$. The illumination (FoI) is fixed to $41° \times 47°$, the FoV can be adjusted by selection of the sensing zone configuration. In general, standard configurations of 3×3, 4×4, 3×6, and 8×8 detection areas can be selected. Further, this sensor features the option to customize the SPAD binning to user defined zone configuration. In our setup, we defined a mode with 7×1 sensing areas. This mode reduces the data acquisition and preprocessing load while providing a maximum horizontal resolution within an FoV of $41° \times 52°$ in air. Due to optical refraction, in the waveguide material, the FoI and FoV is reduced to $29° \times 33.5°$ and $29° \times 37°$, respectively.

A custom electronic board built around an ESP32 microcontroller is used to set the ToF sensor measurement parameters, read data, and synchronize the sensors. This synchronization prevents sensors from interfering with each other when observing the same region of the tactile surface and allows the I2C bus to operate at the maximum read frequency. The number of sensors on the I2C bus, the measurement zones, and laser repetitions mainly influence our data acquisition frequency. For example, with a typical standard configuration of four 4×4 sensing areas, the data acquisition rate is 4.5 samples per second, with each ToF sensor recording 250,000 samples. In the optimized 7×1 mode, the acquisition rate increases by a factor of two to 9 samples per second.

4.2. Tactile map creation

Touch location reconstruction is based on creating a touch likelihood heatmap (a tactile map) by projecting the captured time-of-flight histograms on the surface of the waveguide, considering the time-of-flight of the light and the FoI/FoV of the ToF sensor. For that, we transform the time-of-flight histograms into distance measurements by accounting for the round trip and the speed of light, so distance $d = t\frac{c_1}{2} = t\frac{c}{2n_1}$ where c and c_1 are the speed of light in air and inside the waveguide respectively, and $n_1 = 1.4$ is the waveguide refractive index.

Optics EXPRESS

The tactile map $C(x, y)$ of a ToF sensor in position (x_s, y_s) and whose FoV covers the angles θ_0 to θ_1 (measured with respect to the y-axis) can be reconstructed as

$$\theta = \text{atan2}(x - x_s, y - y_s)$$
$$C(x, y) = \begin{cases} H\left(\frac{2n_1\sqrt{(x-x_s)^2+(y-y_s)^2}}{c_0 n_0}\right) & \text{if } \theta \in [\theta_0, \theta_1] \\ 0 \quad \text{otherwise} \end{cases} \tag{8}$$

where H represents the temporal histogram, either raw ($H(t) = P_r(t)$), with only baseline removal ($H(t) = P_r(t) - B(t)$) or with our full processing ($H(t) = \hat{\beta}_{\text{touch}}(t)$).

Each tactile map $C_i(x, y)$ is created from the histogram $H_i(t)$ corresponding to ToF sensor S_i and assumes that the waveguide is planar or can be approximated to a planar surface (since the thickness of the waveguide is much smaller than its width and height dimensions). Reconstructions involving a setup with multiple ToF sensors around the waveguide can be created by adding the tactile maps $C_i(x, y)$ from each individual ToF sensor. For that, each individual tactile map must be rotated according to the looking direction of each individual ToF sensor. See Supplement 1, Section 2 for a pseudocode algorithm of the tactile map creation.

In the original OptoSkin work, the signal processing for tactile map reconstruction was limited to removing the baseline (Section 3.1), allowing to detect a maximum of two simultaneous touches in the surface of the optical waveguide. In this work, we show how to improve tactile map reconstructions by processing the ToF signal using our proposed algorithm (Section 3), increasing the accuracy of the OptoSkin sensor reconstructions, especially when detecting multiple simultaneous touches and shapes.

5. Performance evaluation

In this section, we evaluate the sensing performance, analyzing both the effect of physical filtering and various signal processing algorithms with our experimental OptoSkin setup in real-world experiments. Particular emphasis is placed on the advantages of our signal processing algorithm, which significantly enhances the sensor's ability to accurately detect and interpret multi-touch and complex shapes inputs. Signal processing is analyzed in three key interaction scenarios: single-touch detection, simultaneous multi-touch detection, and shape reconstruction. All performance evaluation tests were carried out in a room inside a building under standard conditions (approx. 20°C and 40% humidity) and under homogeneous artificial lighting (halogen tubes, 500 lux). Contact interactions involved pressures of approximately $300 g/cm^2$, ensuring sufficient contact with the waveguide's surface to produce FTIR in our OptoSkin setup.

5.1. Ambient light physical filtering

Before analyzing the effect of our signal processing algorithm, we explore the limits of the physical filtering provided by the optical filters of our ToF sensors. For this purpose, we devise a setup involving a 3D printed waveguide, as shown in Fig. 4(a). For the measurements, the entire surface of the waveguide was illuminated with a laboratory white light source consisting of a halogen lamp and a stabilized power supply positioned perpendicular to it. By adjusting the electrical current, we were able to vary the irradiance. In order to address different spectral ranges, visible (< 800 nm) and infrared (>800 nm), optical filters (band pass filter, BPF) were placed in the light path. The contact point on the waveguide was emulated by sticking an adhesive tape to the back of the sensor skin. This allowed us to investigate how the ToF sensor responds to FTIR due to the tape in the presence of varying ambient light. The baseline signal was recorded without ambient light.

Figure 4(b) shows the contact signal (solid lines) from the adhesive tape for different levels of irradiance illumination in the visible range as raw histograms (up) and as processed by our

Optics EXPRESS

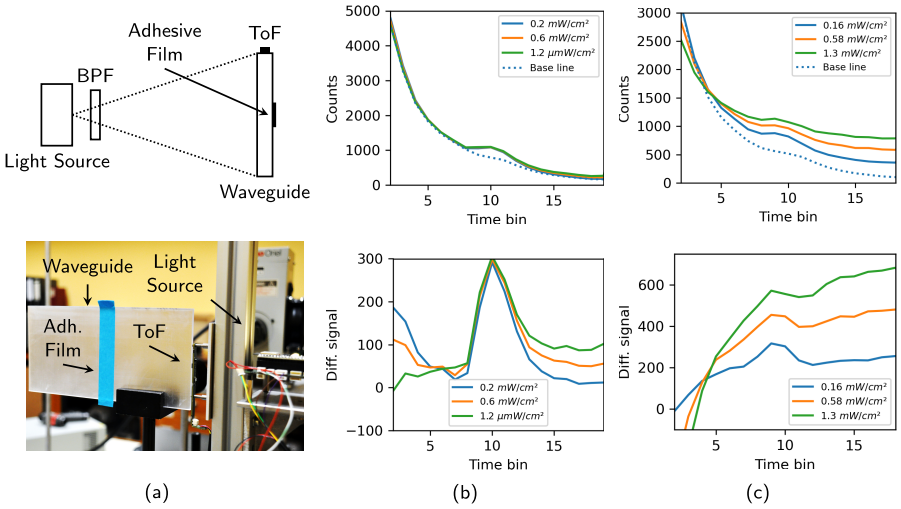

Fig. 4. Experimental investigation of the impact of ambient light in two different spectral ranges. (a) Diagram and photograph of setup, and raw (up) and processed histogram using our algorithm (bottom) for illumination in the visible (b) and infrared (c) spectral range.

algorithm (down). We observe that the sensor response does not change much even at high ambient brightness ($1.2mW/cm^2$). In contrast, Fig. 4(c) shows the influence of ambient light in the infrared range. At low irradiance ($0.16mW/cm^2$) the effect of contact can be observed. With increasing irradiance ($0.58mW/cm^2$ and $1.30mW/cm^2$), more and more devastating effects can be observed on the sensor signal. The increasing ambient light level leads to flattening and vanishing of the contact signature, even when processed. This suggests that our signal processing algorithm would be sensitive to high variations of infrared ambient light, which are nevertheless unlikely in practical scenarios.

5.2. *Single touch localization*

We compare different signal processing algorithms to generate the tactile maps for single touch localization in Fig. 5. Tactile maps using raw histograms do not allow to localize touch since light components like backscattering due to the interface and volume of the waveguide are more predominant than the touch signal, as shown in Fig. 5(b). Only applying the light decay correction (Section 3.2), that accounts for the geometry factor and extinction term, we obtain consistent magnitudes throughout the reconstruction, but light components such as ambient lighting hide touch locations, as shown in Fig. 5(c).

The original OptoSkin work [14] demonstrated single-touch localization using a signal processing pipeline based solely on baseline removal (Section 3.1). Although effective in detecting single-touch events, this approach results in signal magnitudes that can vary by up to two orders of magnitude depending on the distance between the touch location and the ToF sensor that detects it, as shown in Fig. 5(d)-(e). This variability leads to inconsistent tactile maps, with unpredictable signal magnitudes upon touch, and make it challenging to reliably distinguish true contact signals and measurement noise. A similar trend was previously observed in the histogram of Fig. 2(c), highlighting the limitations of relying solely on baseline removal.

Applying both corrections, as proposed in our full signal processing pipeline, illustrated in Fig. 5(f), we reconstruct tactile maps where touch is clearly visible and the intensity variation between close and far touches is significantly reduced compared to the original OptoSkin signal processing [14]. Generating tactile maps with a well-defined and consistent value range is

Optics EXPRESS

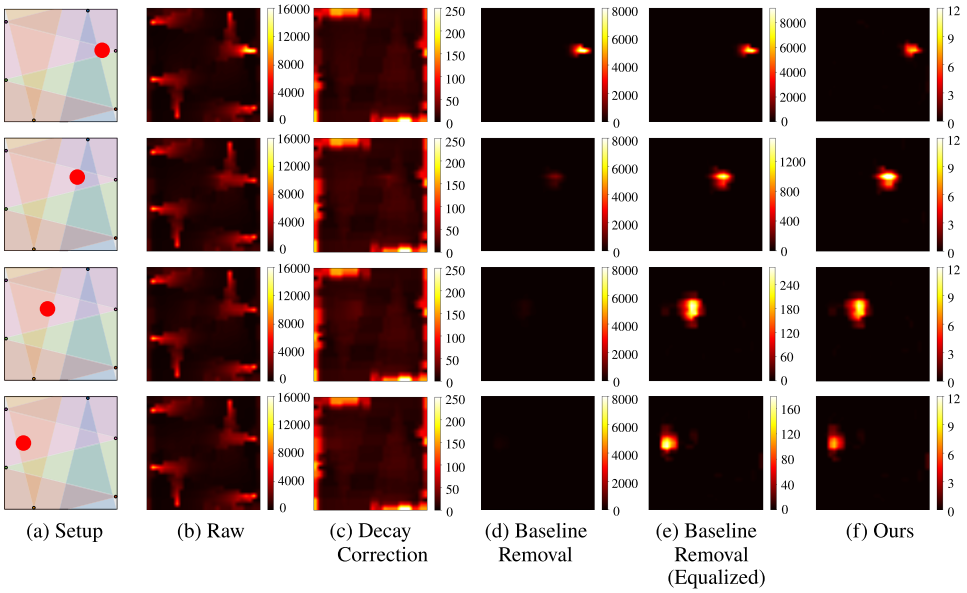

Fig. 5. Reconstructions of single touches at different positions (rows) on our OptoSkin setup (Fig. 3) using various ToF signal processing algorithms. (a) Diagram of the single touch position on the waveguide. (b) Raw: unprocessed measurements exhibit stronger signal close to ToF sensors due to backscattering at the interface β_{int} and within the waveguide volume β_{vol}, obscuring touch events. (c) Decay correction: compensates for light decay, yielding uniform signal magnitudes but failing to reveal touch. (d) Baseline removal: recovers touch locations close to ToF sensors but fails for distant touches due to light decay. Equalizing each reconstruction to its maximum value (e) reveals all the touches, but compromises robustness by losing absolute magnitude information. (f) Ours: produces accurate single-touch maps with consistent magnitudes across different positions.

essential not only for distinguishing true contact signals from noise, but it is also key for enabling reliable detection of multi-touch and complex shape contacts, as we show next.

The total execution time of our signal processing method is below 0.6 *ms* for six ToF sensor histograms. This means that the computational overhead of applying our signal processing is negligible compared to the overall reconstruction pipeline, which takes around 16 *ms*, and ensures the real-time feasibility of the entire system. Furthermore, our algorithm is agnostic to the interaction scenario (single touch, multi-touch or shape reconstruction), as it depends on the ToF sensor temporal histogram bins and waveguide dimensions, which are constant for a given OptoSkin setup. For a more detailed analysis of the execution time of our signal processing algorithm, see Supplement 1, Section 1 and Section 2.

5.3. *Multi-touch localization*

As previously shown, simple baseline removal results in large signal variations due to different distances between the touch location and the ToF sensor. In multi-touch scenarios (Fig. 6(a)), this magnitude difference causes nearby touches to dominate the reconstruction, which yields a stronger signal, and diminishes the visibility of distant touches. This limitation is evident in Fig. 6(b), where multi-touch events far from the ToF sensors are not fully reconstructed, even after equalization to the maximum signal value within the reconstruction, as shown in Fig. 6(c).

In contrast, our method compensates light decay during light propagation, bringing signals from both near and far to comparable magnitudes within the same measurement. This ensures

Optics EXPRESS

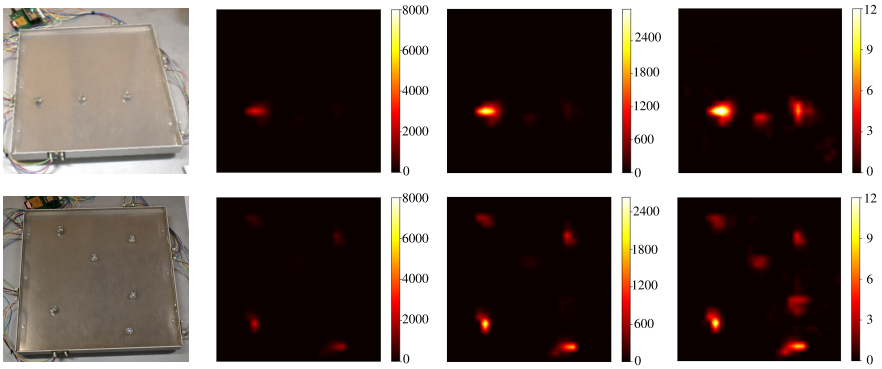

(a) Setup (b) Baseline Removal (c) Baseline Removal (Equalized) (d) Ours

Fig. 6. Multi-touch reconstructions on our OptoSkin setup (Fig. 3) with three (top) and six (bottom) contact points using various ToF signal processing algorithms. (a) Photograph of the setup: three bolts in line and six bolts placed on the sensing surface. (b) Baseline removal: recovers touches close to the ToF sensors but fails to recover distant ones, even after equalizing (c) to the maximum value of the reconstruction. (d) Ours: results in consistent signal magnitudes of close and distant touches, enabling accurate multi-touch reconstructions by aggregating individual reconstructions with comparable magnitudes from each ToF sensor.

that all contact points, regardless of their distance from the ToF sensor, are represented in the final multi-touch tactile map. As a result, our approach, explored in Fig. 6(d), reliably detects all touches across various configurations, which include three bolts in line or six bolts placed on the surface, demonstrating robust multi-touch performance over large sensing areas.

We include a quantitative evaluation of our signal processing algorithm with single touch and multi-touch interactions in Supplement 1, Section 4. This analysis shows the limitations of using raw histograms or applying only decay correction, since they yield low precision and recall as the touch signal is mixed with the baseline signal. Baseline removal improves precision (100% in single touch, $\sim$ 90% in multi-touch), but it struggles with recall (24% in single touch, $\sim$ 60% in multi-touch) since it is not able to detect distant touches. Our full signal processing algorithm significantly enhances performance by normalizing the magnitude of both close and far touches. This results in high precision (100% in single touch, $\sim$ 98% multi-touch) and substantially improved recall (100% single-touch, $\sim$ 92% multi-touch). Our algorithm achieved an average distance error of 0.86 *cm* for estimated touches, which is comparable to the ToF sensor's inherent distance resolution of approximately 1.1 *cm*.

5.4. Shape reconstruction

Recognizing the shape of objects in contact with the optical waveguide surface is challenging due to varying distances between different object regions and the surrounding ToF sensors. When a shape touches the optical waveguide, multiple sensors detect the event simultaneously. However, areas closer to the ToF sensors produce significantly stronger signals, as discussed before. This leads to imbalanced reconstructions where nearby regions dominate and distant ones are underrepresented, and only partial or distorted reconstructions of the object's shape can be obtained.

We evaluate shape reconstruction using a stick placed in three positions and an upside-down mug, shown in the photographs in Fig. 7(a). With only baseline removal, in Fig. 7(b) we show that the dominance of the signal corresponding to areas closer to the ToF sensors is evident. Even

Optics EXPRESS

when equalizing to the maximum value within each individual reconstruction, shown in Fig. 7(c), only high-intensity hotspots remain, making shape identification unreliable.

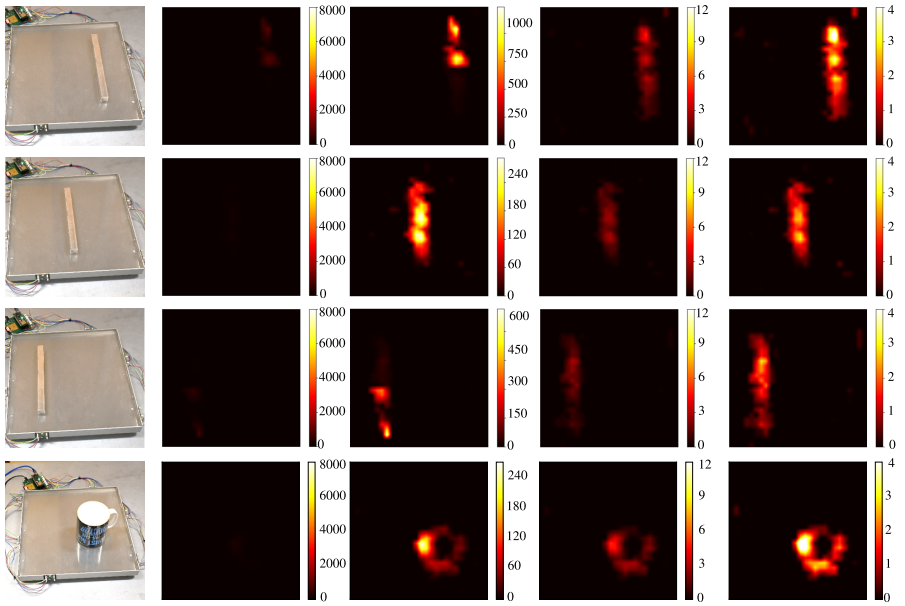

Fig. 7. Shape reconstructions using various ToF signal processing methods. (a) A stick in three positions and an upside-down mug are placed on the OptoSkin surface. Each object is simultaneously detected by multiple ToF sensors. (b) Baseline removal alone yields reconstructions dominated by regions closer to the ToF sensors, and obscuring the overall shape. (c) Equalizing each individual reconstructions reveals more hotspots but shapes reconstructions remain inconsistent due to unbalanced magnitudes across ToF sensors. (d) Our algorithm compensates for light decay across the waveguide, producing balanced contributions from all sensors and enabling a more complete and geometrically accurate reconstructions. Notably, the rim and central hole of the mug are partially reconstructed. The mug appears more intense than the stick due the same applied force being distributed on a smaller contact area, resulting in higher pressure. (e) For visualization, equalizing the reconstructions with our processing algorithm highlights the preserved shape details and demonstrates robustness across varying contact areas.

By compensating using our approach (baseline removal and light decay compensation), our method balances the contributions of all ToF sensors, both across and within individual reconstructions, regardless of their distance to the object. As shown in Fig. 7(d), this results in more complete and accurate reconstructions: the stick is fully visible along its length and the circular rim of the upside-down mug is preserved. Shape reconstructions with our approach differ in magnitude with respect to single and multi-touch reconstructions, reflecting variations in pressure, since all tests were performed with the same force, but the stick and mug's larger contact area reduced the pressure applied. This suggests that our approach is consistent with respect to the amount of applied pressure. Furthermore, by equalizing the tactile map for visualization purposes, in Fig. 7(e), we show that our approach accurately reconstructs the stick's shape in all positions and the circular rim of the mug.

Optics EXPRESS

6. Discussion

In this work, we analyze time-of-flight light transport within waveguides and formulate a forward model to describe it. We then invert this model to introduce a real-time signal processing algorithm that corrects raw ToF signals from FTIR sensors. Our evaluation on an OptoSkin setup demonstrates that our algorithm improves contact detection, particularly for detecting multiple simultaneous touches and reconstructing the shape of objects in contact with the tactile sensor. In these scenarios, the light signal is dominated by contact areas close to the ToF sensors and distant contact areas are not reconstructed. Our algorithm compensates this effect, showing consistent tactile maps regardless of the touch distance from the ToF sensor.

While we have presented quantitative metrics on our signal processing algorithm's performance within the OptoSkin framework, a direct, comprehensive comparison with diverse tactile sensing technologies is not straightforward. Other tactile sensing technologies usually achieve better distance error metrics but are bulkier (e.g., large-area vision based [17]), or have difficulties being adapted to irregular surfaces or having multi-touch capabilities (e.g., capacitive [26] or resistive [27]). We refer to the original OptoSkin [14] paper for a comparison between tactile sensing technologies. Our OptoSkin demonstrator was built as a prototype for comparing signal processing methods and not for achieving the best quantitative metrics, although we believe the results presented here allow to consider ToF FTIR-based tactile sensors as an interesting option for sensing large areas.

Our forward model assumes that the optical properties of the setup are known, including refractive index, scattering and absorption coefficients, or the ToF sensor characteristics. Additionally, our signal processing algorithm relies on a one-time baseline acquisition during system startup, presuming stable environmental conditions. To further enhance the robustness and broader applicability of our approach, several promising avenues for research exist:

More complete physical model Effects such as partial reflections (light escaping the waveguide) and wave optics effects have not been considered in our forward model, which might be an interesting avenue for future research. Still, our experiments suggest that our model is very complete as it can be used to eliminate most of the misleading effects of ToF signals.

Improved multi-touch capabilities Another interesting direction for future work involves addressing the "shadowing" effect that occurs when multiple touches at different distances are detected by the same ToF sensor. Since the light scattered by any touch point does not continue propagating, closer touch points, which scatter more light, can reduce the amount of light reaching further touch zones. Our results show that this effect, even if present, does not degrade the signal enough to prevent the detection of further contact points. Nevertheless, developing compensation techniques specifically tailored for multiple contact points per ToF sensor could enhance multi-touch detection and shape reconstruction performance in complex sophisticated scenarios.

Environmental conditions: lighting changes Our experiments with varying ambient light show that ToF signals and touch reconstructions degrade as the intensity of ambient light, at the sensor's operating wavelength, increases. This suggests that the sensor's performance might be sensitive to large variations of infrared ambient light, which would happen in specific situations like moving the sensor from an indoor to an outdoor environment while active. However, we have found our system is robust to typical indoor illumination changes, where infrared ambient light changes are low.

To address indoor to outdoor lighting changes, future efforts could explore solutions like applying infrared-blocking coating to the waveguide surface to filter out external infrared illumination, or conducting an extensive measurement benchmark to characterize the baseline signal evolution across a diverse illumination spectra. Such data would enable dynamic baseline adjustments based on real-time environmental light sensing. Another approach involves covering the waveguide with an opaque flexible material (e.g., a fabric), and performing touch detection

Optics EXPRESS

due to temporary waveguide deformation rather than FTIR. While this limits applicability to soft waveguides, it offers an alternative for challenging lighting environments. Of these, the infrared-blocking coating presents the more versatile solution for hard and soft waveguide materials.

Environmental conditions: temperature, humidity and mechanical stress While environmental conditions, like temperature or humidity, can alter the waveguide material optical properties, we anticipate minimal changes within typical operating ranges (e.g., $-10°C$ to $+40°C$), with studies showing that refractive index changes due to temperature $\Delta n/\Delta T$ are in the order of $10^{-4}\ °C^{-1}$ [28]. The reason is that silicones are generally known for their high thermal stability and low water absorption (see Supplement 1, Section 3). In any case, a comprehensive characterization of waveguide material properties under various environmental conditions would enable dynamic model adjustments.

Temperature, humidity, and mechanical stress contribute to the wear and aging of silicone rubber, which would require updating the baseline signal. However, these degradations occur slowly over time and can be accounted for by the initial startup calibration. Moreover, silicone materials are used in harsh environments [29], so we expect the mechanical stress induced by touch interactions to be acceptable.

Optical properties of the waveguide Our OptoSkin sensor uses a waveguide material with relatively low scattering and absorption coefficients, enabling light to propagate further with minimal attenuation. However, the sensing range is ultimately limited by the geometric factor and transmittance term, which is directly related to the absorption and scattering coefficients. Future research could explore waveguide materials with even lower scattering and absorption for extended sensing ranges. A detailed discussion on the evolution of the signal-to-noise ratio (SNR) with increasing distance from ToF sensors is provided in the Supplement 1, Section 5. Also, this work assumes predominantly straight-line light propagation thanks to the low scattering coefficient of the waveguide, but using materials with higher scattering coefficients might necessitate leveraging techniques from time-of-flight imaging through highly scattering media [30,31].

Data driven techniques Our proposed signal processing for detecting touch is physically-based, offering interpretability and reduced reliance on extensive data. While data-driven approaches, such as machine learning, could enhance adaptability to varied sensor and environmental conditions, they typically demand significant data collection. Our proposal of collecting data for adjusting the baseline to changing environmental conditions (lighting, temperature, humidity, mecahanical stress) is a way of incorporating data-driven techniques into our physically-based model. A promising future direction involves Physics-Informed Neural Networks (PINNs), which could leverage physical priors to achieve robust adaptability with less data.

Application to other domains Even tough our experiments are tailored to OptoSkin, a ToF FTIR-based tactile and pressure sensor, our proposed signal processing algorithm is applicable to any ToF signal in participating media, such as water or fog. This opens promising avenues for future work in applications such as underwater imaging, fog-penetrating detection, and other sensors based on total internal reflection. We hope our contribution inspires future research in these other domains.

Funding. Ministerio de Ciencia, Innovación y Universidades (FPU23/03132); European Commission's HORIZON EUROPE Research and Innovation Actions (101070310).

Acknowledgment. This work has received funding from the European Commission's HORIZON EUROPE Research and Innovation Actions project Sestosenso under GA number 101070310. Jorge Garcia-Pueyo was supported by the FPU23/03132 predoctoral grant.

Disclosures. The authors declare no conflicts of interest.

Data availability. Code and data underlying the results presented in this paper are available in Ref. [32].

Supplemental document. See Supplement 1 for supporting content.

Optics EXPRESS

References

1. W. Zheng, K. Liu, D. Guo, *et al.*, "A large-area tactile sensor for distributed force sensing using highly sensitive piezoresistive sponge," in *International Conference on Robotics and Automation* (IEEE, 2024), pp. 1063–1069.
2. F. Giovinazzo, F. Grella, M. Sartore, *et al.*, "From cyskin to proxyskin: Design, implementation and testing of a multi-modal robotic skin for human-robot interaction," Sensors **24**(4), 1334 (2024).
3. H. Hu, C. Zhang, X. Lai, *et al.*, "Large-area magnetic skin for multi-point and multi-scale tactile sensing with super-resolution," npj Flexible Electron. **8**(1), 42 (2024).
4. T. Pereira, S. Rusinkiewicz, and W. Matusik, "Computational light routing: 3d printed optical fibers for sensing and display," ACM Trans. Graph. **33**(3), 1–13 (2014).
5. B. Ward-Cherrier, N. Pestell, L. Cramphorn, *et al.*, "The tactip family: Soft optical tactile sensors with 3d-printed biomimetic morphologies," Soft Rob. **5**(2), 216–227 (2018).
6. R. Li, R. Platt, W. Yuan, *et al.*, "Localization and manipulation of small parts using gelsight tactile sensing," in *IEEE/RSJ International Conference on Intelligent Robots and Systems* (2014), pp. 3988–3993.
7. M. Lambeta, G. Kammerer, D. Jayaraman, *et al.*, "Digit: A novel design for a low-cost compact high-resolution tactile sensor with application to in-hand manipulation," IEEE Robotics and Automation Letters **PP**, 1 (2020).
8. J. Y. Han, "Low-cost multi-touch sensing through frustrated total internal reflection," in *Proceedings of the 18th Annual ACM Symposium on User Interface Software and Technology* (Association for Computing Machinery, 2005), pp. 115–118.
9. R. Wattanaparinton and K. Takemura, "Vision-based tactile sensing using multiple contact images generated by re-propagated frustrated total internal reflections," in *International Conference on Systems, Man, and Cybernetics* (IEEE, 2022), pp. 962–967.
10. R. Hu, H. Yang, L. Wang, *et al.*, "Flexible optical tactile sensor based on a liquid-membrane lens structure," Appl. Opt. **62**(26), 6952–6960 (2023).
11. T. Xu, L. Li, Y. Wang, *et al.*, "Highly sensitive soft optical fiber tactile sensor," Opt. Express **30**(19), 34064–34076 (2022).
12. L. Li, F. Yang, Q. Ma, *et al.*, "Integrating an optical fiber sensor and artificial intelligence for enhanced tactile sensing in human-computer interaction," Optica **12**(2), 263–273 (2025).
13. J.-T. Lin, C. A. Newquist, and C. K. Harnett, "Multitouch pressure sensing with soft optical time-of-flight sensors," IEEE Trans. Instrum. Meas. **71**, 1–8 (2022).
14. E. Bacher, S. Cartiel, J. García-Pueyo, *et al.*, "Optoskin: Novel lidar touch sensors for detection of touch and pressure within wave guides," IEEE Sens. J. **24**(20), 33268–33280 (2024).
15. U. Wandinger, *Introduction to Lidar* (Springer, 2005), pp. 1–18.
16. J.-H. Lee and C.-H. Won, "High-resolution tactile imaging sensor using total internal reflection and nonrigid pattern matching algorithm," IEEE Sens. J. **11**(9), 2084–2093 (2011).
17. A. Lavatelli, A. Zanoni, E. Zappa, *et al.*, "On the design of force sensors based on frustrated total internal reflection," IEEE Trans. Instrum. Meas. **68**(10), 4065–4074 (2019).
18. H. Krauss and K. Takemura, "Stretchable optical waveguide sensor capable of two-degree-of-freedom strain sensing mediated by a semidivided optical core," IEEE/ASME Transactions on Mechatronics **27**(4), 2151–2157 (2022).
19. J. Hu, D. Cao, Y. Li, *et al.*, "Polymer-based optical waveguide tactile sensing method for 3-d surfaces," IEEE Sens. J. **23**(8), 8761–8768 (2023).
20. A. Maccarone, K. Drummond, A. McCarthy, *et al.*, "Submerged single-photon lidar imaging sensor used for real-time 3d scene reconstruction in scattering underwater environments," Opt. Express **31**(10), 16690–16708 (2023).
21. M. Shangguan, Y. Li, Y. Mo, *et al.*, "Compact underwater single-photon imaging lidar," Opt. Lett. **50**(6), 1957–1960 (2025).
22. K. Walcarius, J. Rosin, L. Hespel, *et al.*, "Impact of blur on 3d laser imaging: Monte-carlo modelling for underwater applications," Opt. Express **31**(16), 26194–26207 (2023).
23. J. Xian, D. Sun, S. Amoruso, *et al.*, "Parameter optimization of a visibility lidar for sea-fog early warnings," Opt. Express **28**(16), 23829–23845 (2020).
24. T. Factory, "TFC4190-T19," https://trollfactory.de/Produkte/Silikon-Kautschuk/Haertegrad-Shore/weich-Shore-A25/TFC4191/TFC-Silikon-Kautschuk-Typ-19-transparent-Shore-1-1-Special-Effect-Groesse-1kg-2x500g (2025).
25. AMS-OSRAM, "TFM8828," https://ams-osram.com/products/sensor-solutions/direct-time-of-flight-sensors-dtof/ams-tmf8828-configurable-8x8-multi-zone-time-of-flight-sensor (2025).
26. A. Pagoli, F. Chapelle, J. A. Corrales-Ramon, *et al.*, "Large-Area and Low-Cost Force/Tactile Capacitive Sensor for Soft Robotic Applications," Sensors (Basel, Switzerland) **22**(11), 4083 (2022).
27. Y. Zhu, Y. Liu, Y. Sun, *et al.*, "Recent advances in resistive sensor technology for tactile perception: A review," IEEE Sens. J. **22**(16), 15635–15649 (2022).
28. Z. Zhang, P. Zhao, P. Lin, *et al.*, "Thermo-optic coefficients of polymers for optical waveguide applications," Polymer **47**(14), 4893–4896 (2006).
29. M. Yazdan Mehr, W. Van Driel, F. De Buyl, *et al.*, "Study on the degradation of optical silicone exposed to harsh environments," Materials **11**(8), 1305 (2018).
30. P. Luesia, M. Crespo, A. Jarabo, *et al.*, "Non-line-of-sight imaging in the presence of scattering media using phasor fields," Opt. Lett. **47**(15), 3796–3799 (2022).

Optics EXPRESS

31. D. S. Jeon, A. Meuleman, S.-H. Baek, *et al.*, "Polarimetric iToF: Measuring High-Fidelity Depth Through Scattering Media," in *IEEE/CVF Conference on Computer Vision and Pattern Recognition* (IEEE Computer Society, 2023), pp. 12353–12362.
32. J. García-Pueyo, "TimeOfFlightSignalProcessingFTIRTactileSensors," GitHub (2025), https://github.com/jgarciapueyo/TimeOfFlightSignalProcessingFTIRTactileSensors.